

# Development and Performance Evaluation of a Time-of-Flight Positron Emission Tomography Detector Based on a High-Quantum-Efficiency Multi-Anode Photomultiplier Tube

Jeong-Whan Son, Guen Bae Ko, Jun Yeon Won, Hyun Suk Yoon, and Jae Sung Lee

**Abstract**—We present the development and performance evaluation of time-of-flight (TOF) positron emission tomography (PET) detector modules designed for a proof-of-concept prototype of a TOF PET scanner based on the advanced high-quantum-efficiency (high-QE) multi-anode photomultiplier tube (PMT) (Hamamatsu H10966A-100 with super-bialkali photocathode) coupled with LGSO scintillation crystals (3 mm × 3 mm × 20 mm) whose cross section is smaller than that of crystals used in current clinical scanners. Compact dedicated front-end analog electronics combined with the high packing density and large effective area of the multi-anode PMT allow a modular detector design and thus a flexible and extendible geometry of the PET system. We optimized the electrical parameters (trigger threshold level, high voltage of PMTs, and amplifier gain) to yield the best timing resolution and acquired excellent flood map quality, energy resolution, and timing resolution with the optimal setup; the average distance-to-width ratio (DWR) of crystal peaks for 40 detectors was  $5.3 \pm 1.0$ , and the average energy resolution and coincidence resolving time (H10966A-100 vs. H10966A-100) were  $11.04 \pm 0.80\%$  (FWHM) and  $341 \pm 45$  ps (FWHM) respectively. The detector modules developed in this study and optimized their parameters to yield the best detector performance will be useful for the future development of the next generation TOF PET scanners based on them.

**Index Terms**—Hamamatsu H10966A-100, LGSO, multi-anode photomultipliers, time-of-flight (TOF) PET.

## I. INTRODUCTION

**I**N POSITRON emission tomography (PET) studies, the measurement of the arrival time difference of coincident gamma-ray pairs (time-of-flight (TOF) information) allows more accurate localization of positron emitters on the line-of-response (LOR), leading to improved reconstructed PET image quality [1]–[3]. Propagation of image noise along the LOR during the projection process in image reconstruction is limited within a restricted space (segmented LOR) using the TOF information, enhancing the signal-to-noise ratio (SNR) of

PET images [4]. Accordingly, the TOF measurement improves the diagnostic power of PET and/or reduces the scan time or radiation dose [5], [6]. Another benefit of TOF information is the mitigation of image artifacts due to inconsistent or missing data in PET measurements [7], [8]. In addition, the joint estimation of activity and attenuation data can be facilitated by the improved TOF measurement, and is useful in reducing artifacts due to the misalignment of emission and transmission data and ultimately eliminating the necessity of transmission data for PET attenuation correction [9], [10].

The SNR gain of PET images due to TOF information can be calculated as  $\sqrt{D/k \cdot \Delta x}$ , where  $D$  is the effective diameter of the scanned subject,  $\Delta x$  the positional uncertainty of a positron emitter that is determined by the timing resolution of the PET system, and  $k$  the variable determined by the TOF kernel shape and filters used in reconstruction process [4], [11], [12]. Although this estimation of TOF gain is accurate at the center of a uniform object reconstructed using an analytic algorithm, the SNR in non-uniform objects and iterative algorithms is also improved with better timing resolution [1], [3], [13]. To achieve better timing resolution of scintillation detectors used in PET systems, scintillation crystals should yield more light photons as quickly as possible and photo-sensors should measure the photons with high photon detection efficiency, a fast response time, and a low transit time spread [14]–[16]. The TOF PET detectors (so-called block detectors and quadrant-sharing detectors) conventionally used in clinical PET and PET/computed tomography (CT) systems comprise an array of segmented Lu-based scintillation crystals (i.e., LSO, LYSO, and LGSO) and multiple single- or four-anode photomultiplier tubes (PMTs) [17]–[19]. However, the minimum usable crystal size is limited because the two-dimensional distribution of light photons generated from a large number of crystals is measured by only the small number of PMTs. Many light photons are also lost because of the gap between the effective (light-sensitive) areas of PMTs, leading to the degradation of the intrinsic spatial and timing resolutions of the detector.

Two complementary approaches that can be taken to advance TOF PET detectors are the use of silicon photomultipliers (SiPMs) and the use of position-sensitive multi-anode PMTs. The compactness of a SiPM allows the one-to-one coupling of the scintillation crystal and photo-sensor, which enriches the light collection and enhances the signal properties. The

Manuscript received May 28, 2015; revised October 04, 2015; accepted December 23, 2015. Date current version February 16, 2016.

J.-W. Son, G. B. Ko, J. Y. Won, and H. S. Yoon are with the Department of Nuclear Medicine and Biomedical Sciences, Seoul National University, Seoul 110-744, Korea.

J. S. Lee is with the Department of Nuclear Medicine, Biomedical Sciences and Institute of Radiation Medicine, Seoul National University, Seoul 110-744, Korea (e-mail: jaes@snu.ac.kr).

Color versions of one or more of the figures in this paper are available online at <http://ieeexplore.ieee.org>.

Digital Object Identifier 10.1109/TNS.2015.2514118

magnetic-resonance-compatibility of this sensor has also led to the development of a PET/magnetic resonance imaging scanner with TOF measurement capability. On the other hand, the position-sensitive multi-anode PMT is much less vulnerable to fluctuations in temperature and supply voltage in contrast to the SiPM. A lower dark count rate and higher SNR at room temperature [20] is another advantage of the multi-anode PMT over the SiPM for TOF PET as these properties allow a large multiplexing ratio of output channels and a low trigger threshold for signal pickup and timing measurement. The better radiation hardness of the PMT compared with the SiPM is the reason why the PMT is preferred in TOF PET systems for hadron-therapy monitoring.

As the next generation TOF PET scanners require higher spatial resolution and more advanced functions (i.e., concurrent measurement of the depth-of-interaction (DOI) and TOF information) than current scanners, a multi-anode PMT with small pixel size, large effective area, high packing density (effective area/full dimension), good timing performance, and moderate cost is favored. The Hamamatsu H10966A-100 is such an advantageous multi-anode PMT equipped with a super-bialkali (SBA) photocathode that yields higher blue sensitivity index (BSI) and quantum efficiency (QE) than the H8500, the conventional and widely used multi-anode PMT equipped with a bialkali (BA) photocathode. In addition, the PMT has fewer dynode stages than other multi-anode PMTs, leading to less transit time and transit time jitter. It has been also shown that the high-QE of H10966A-100 has the benefit for resolving small crystals [21], [22].

The ultimate goal of our investigation is the development of a proof-of-concept prototype of a TOF PET scanner based on this advanced multi-anode PMT, the H10966A-100, coupled with LGSO scintillation crystals with a front surface size (3 mm × 3 mm × 20 mm) smaller than that of crystals currently used in most clinical scanners [17], [18], [23]–[27]. The study developed a detector module and optimized their parameters (trigger threshold level, high voltage of PMTs, and amplifier gain) to yield the best timing resolution. The optimal setup was finally applied to 40 detector modules to confirm the feasibility of a single PMT-ring TOF PET system under development.

## II. MATERIALS AND METHODS

### A. Photomultipliers

We used an H10966A-100 high-QE multi-anode (8 × 8) PMT (Hamamatsu Photonics K. K., Hamamatsu, Japan) with 64 anode outputs and a single last dynode output. Table I compares the main characteristics of several flat-panel multi-anode PMTs with the same dimensions provided by Hamamatsu Photonics. The H10966A-100 employs an SBA photocathode, which yields a higher BSI (13.5) and QE (34.1%@420 nm) than conventional multi-anode PMTs with BA photocathodes. With higher QE, the PMT generates more photoelectrons per single event leading to improved time performance [28]. Additionally, less transit time jitter is expected considering fewer dynode stages (eight stages) and lower transit time of the H10966A-100 compared with other multi-anode PMTs (10–12 stages) [29].

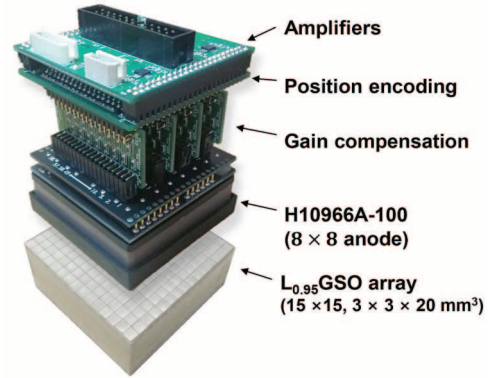


Fig. 1. Developed PET detector. The compact electronics allow a modular detector design that is suitable for building a PET scanner.

### B. TOF PET Detector Design

For the TOF PET system with diameter > 60 cm, spatial resolution of 3–4 mm, good sensitivity, modular design, and gap between detectors < 2 crystals, we developed PET detectors consist of a scintillation crystal array, a PMT, and electronics as shown in Fig. 1. LGSO ( $\text{Lu}_{1.9}\text{Gd}_{0.1}\text{SiO}_4\text{:Ce}$ ; Hitachi Chemical Co., Japan) scintillation crystals (3 mm × 3 mm × 20 mm) were used with all surfaces chemically polished. The crystals were arranged in a 15 × 15 array with a crystal pitch of 3.1 mm. The size of the crystal array was therefore 46.4 mm × 46.4 mm × 20 mm, which is only slightly smaller than the effective area of the PMT (49 mm × 49 mm), allowing an appropriate modular detector design to be implemented in the PET scanner. Each crystal was surrounded by enhanced specular reflectors (> 98% reflectance, 0.065 mm thickness; 3M, USA) except for one surface that was in contact with the PMT window. The crystal array and PMT were coupled with optical grease (BC-630; OKEN, Japan) to minimize light loss during the transition from crystal to PMT.

Dedicated electronics including a gain compensator, a position encoder, and amplifiers were implemented. A gain compensation circuit was used to mitigate the gain non-uniformity of PMT anodes, which had a maximum/minimum ratio of up to 2.7 [30]. The 64 gain-compensated anode signals were then multiplexed into four position-encoded signals (A, B, C, and D) using a resistive charge division network [30]–[32]. The gamma-ray interaction position was later determined using (1) and (2).

$$\mathbf{X} = \frac{\mathbf{A} + \mathbf{B} - \mathbf{C} - \mathbf{D}}{\mathbf{A} + \mathbf{B} + \mathbf{C} + \mathbf{D}} \quad (1)$$

$$\mathbf{Y} = \frac{\mathbf{A} - \mathbf{B} - \mathbf{C} + \mathbf{D}}{\mathbf{A} + \mathbf{B} + \mathbf{C} + \mathbf{D}} \quad (2)$$

The position-encoded signals were amplified by fully differential amplifiers so that transmission noise cancelled out [33], [34]. The gamma-ray arrival time information was derived from a dynode signal. The dynode signal was magnified through an ultrahigh-speed (1.5 GHz bandwidth, 4100 V/μs slew rate) current feedback operational amplifier. Trigger signals were generated using a comparator as a leading edge discriminator by comparing dynode signals with the predetermined threshold voltage and fed into the following time-to-digital converters (TDCs). The threshold voltage was generated using a digital-to-analog converter (0.61 mV granularity), and the voltage was regulated

TABLE I  
MAIN CHARACTERISTICS OF HAMAMATSU  $8 \times 8$  MULTI-ANODE PMTs

	H10966A-100	H10966	H12700	H8500
Rise time [ns]	0.4	0.4	0.65	0.4
Gain (Typ.)	$3.2 \times 10^5$	$3.3 \times 10^5$	$1 \times 10^6$	$1.5 \times 10^6$
Dynode stages	8	8	10	12
Transit time [ns]	4	4	5.3	6
Transit time jitter [ps]	N/A <sup>a</sup>	N/A <sup>a</sup>	280	400
Photocathode	Super-bialkali	Bialkali	Bialkali	Bialkali
Blue sensitivity index (Typ.)	13.5	9.5	12	9.5
Quantum efficiency (420 nm) [%]	34.1 <sup>b</sup>	24 <sup>c</sup>	30.3 <sup>b</sup>	24 <sup>b</sup>
Dimension [mm]	$52 \times 52$	$52 \times 52$	$52 \times 52$	$52 \times 52$
Effective area [mm]	$49 \times 49$	$49 \times 49$	$48.5 \times 48.5$	$49 \times 49$
Anode size [mm]	$5.8 \times 5.8$	$5.8 \times 5.8$	$6 \times 6$	$5.8 \times 5.8$
Peak wavelength [nm]	400	400	400	400

<sup>a</sup> No measured transit time jitter data <sup>b</sup> Estimated from quantum efficiency of H10966 and blue sensitivity index difference <sup>c</sup> Measured by Hamamatsu Photonics K. K.

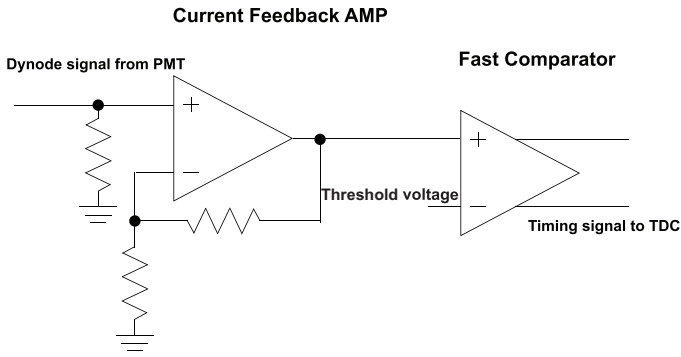


Fig. 2. Simplified circuit for generating timing signals from dynode signals of a PMT.

by a microcontroller which was communicated through RS-232 protocol. The circuit design for timing signals is shown in Fig. 2.

### C. Data Acquisition Setup

To evaluate the performance of the developed PET detector, we used a reference detector comprising a single channel PMT (R9800; Hamamatsu Photonics K. K., Hamamatsu, Japan) coupled with a LYSO ( $\text{Lu}_{1.8}\text{Y}_{0.2}\text{SiO}_5:\text{Ce}$ ;  $4 \text{ mm} \times 4 \text{ mm} \times 10 \text{ mm}$ ) scintillation crystal. Using (3), with known single timing resolution of the reference detector ( $\Delta T_b = 255 \text{ ps}$ ) and measured timing resolution between the reference detector and the developed detector ( $\Delta T_{a-b}$ ), the coincidence resolving time (CRT) of the pair of developed detectors (H10966A-100 vs. H10966A-100) was calculated as  $\sqrt{2} \times \Delta T_a = \sqrt{2 \times (\Delta T_{a-b}^2 - \Delta T_b^2)}$ .

$$\Delta T_{a-b}^2 = \Delta T_a^2 + \Delta T_b^2 \quad (3)$$

A block diagram illustrating the measurement setup is shown in Fig. 3. The distance between the reference detector and the developed detector was 20 cm, and a  $^{22}\text{Na}$  point source ( $13.6 \mu\text{Ci}$ ) was positioned in front of the reference detector for coincidence acquisition.

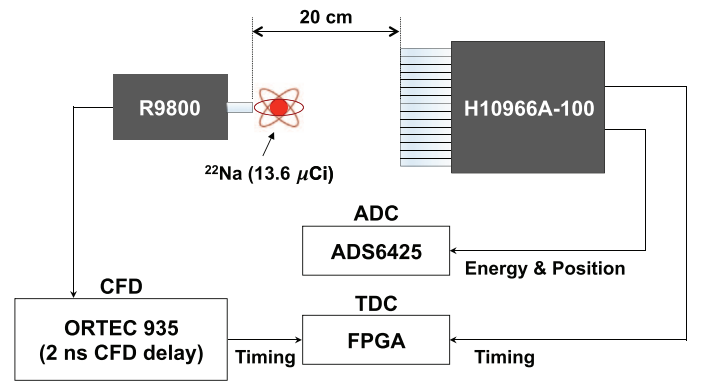


Fig. 3. Experimental setup for coincidence data acquisition.

Time stamps were generated from the FPGA-based dual-phase tapped-delay-line TDC that was implemented on a Virtex-6 device (ML605; Xilinx, USA) [35]. Event processing time for determining the time stamp (i.e., latency) was 47.5 ns. The arrival time was estimated on a personal computer from the time stamps. The TDC has 10 ps resolution, 12.8 ps measurement uncertainty of time interval, and 200 MSa/s maximum conversion rate. It also has the on-the-fly calibration capability for correcting the nonlinearity of TDC caused by process, voltage and temperature variations.

Data were acquired using a custom-built FPGA-based data acquisition (DAQ) system [36]. The position signals were sampled at 125 MSa/s with 12-bit resolution using pipeline analog-to-digital converters (ADS6425; Texas Instrument, USA). When the TDC received a trigger signal from a detector, the TDC transmitted a trigger signal to the DAQ system in 20 ns. Once receiving a trigger signal from the TDC, the DAQ system started to integrate the delayed position signals of the triggered channel for 200 ns to obtain the energy information. The energy of each position signal and the sum of the energies were calculated in real time with the DAQ system (took  $216 \text{ ns} = \text{integration time} + 16 \text{ ns}$ ). Meanwhile, the TDC

determined the arrival time and transmitted the information to the DAQ system via a GTX transceiver (took about 300 ns). If the triggered channel and the channel information (i.e., channel ID) received through a GTX transceiver were matched (took about 16 ns), the DAQ system synced the energy and time information and transferred the data to a personal computer.

#### D. Optimization of Time Performance

To achieve the best timing resolution of the developed PET detectors, we optimized three major electrical parameters that determine timing resolution (i.e., the threshold voltage, high voltage applied to PMTs, and dynode amplifier gain). The CRT was estimated with five different threshold levels (3%, 5%, 7%, 10%, and 15% of the average 511-keV dynode pulse peak voltage) and five different high voltages (900, 950, 1000, 1050, and 1100 V) of a PMT. With the optimized threshold level and high voltage, the CRT was estimated for different dynode amplifier gains (from  $\times 5$  to  $\times 95$ ) using three randomly selected PMTs with different gains. The optimal setup was then applied to 40 detector modules for the evaluation of the average performance.

For each experimental setup, 6.5 million coincidence events were acquired. Flood images were composed using all data including those of scattered events. Energy histograms were generated for individual crystals and relative energy peaks and energy resolutions were calculated. Energy and timing resolutions were calculated as the full-width-at-half-maximum from Gaussian fits to the histograms.

### III. RESULTS

#### A. Optimal Setup for Time Performance

The optimal threshold level, high voltage, and amplifier gain for randomly selected detectors were 5% of the average 511-keV dynode pulse peak voltage, 1100 V (i.e., the maximum value recommended by the manufacturer), and  $\times 20$ , respectively, as shown in Fig. 4 (The time performances of these three detectors ranked top 15, 33, and 60% out of 40 detectors.). In Fig. 4, each point represents the average value of 225 crystals in one detector. All three detectors with different gains ( $0.25$ ,  $0.22$ , and  $0.13 \times 10^6$ ) showed same trend. We used 100 V higher high voltage value than that recommended by manufacturer (1000 V) in order to achieve the best timing performance although there is a concern that increasing high voltage may cause increasing dark count noise and shorten lifetime of PMT. With the recommended high voltage (1000 V), approximately 20 ps timing resolution degradation is expected as shown in Fig. 4(a).

The best CRT acquired by the optimization was 312 ps, and one-dimensional and two-dimensional CRT histograms of the detector are shown in Fig. 5(a). The better CRTs in the central region were mainly due to a greater number of detected light photons, which will be discussed in Section III-C.

#### B. Flood Images

The two-dimensional position histogram was acquired with the uniform irradiation of 511-keV gamma-rays from a  $^{22}\text{Na}$  point source. In Fig. 6, all  $15 \times 15$  scintillation crystals

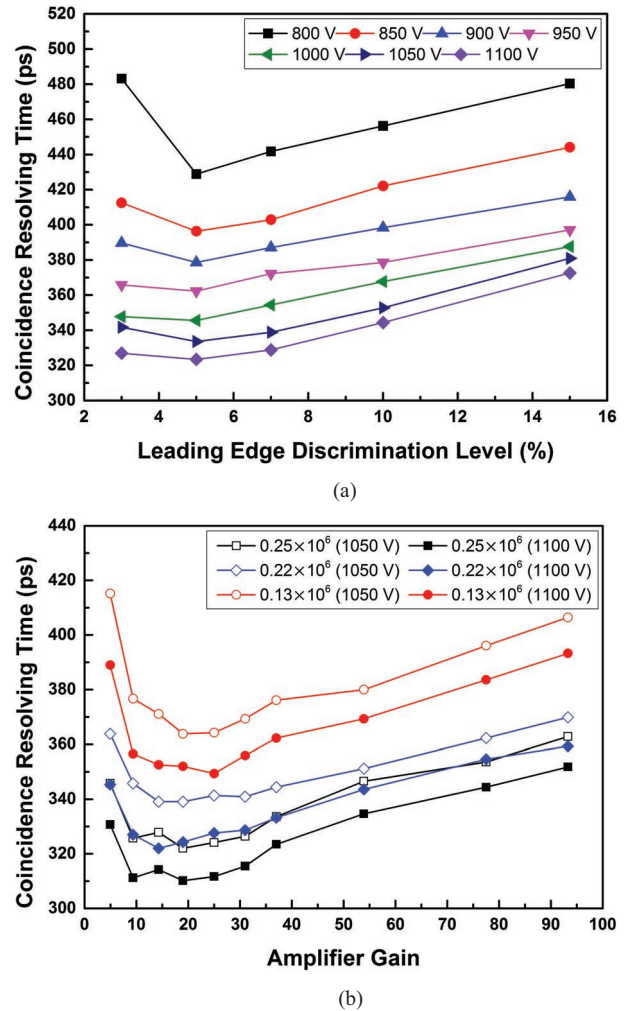


Fig. 4. Average coincidence resolving time of 225 crystals (a) with different threshold levels and high voltages using the best detector (top 15%) among the three randomly selected detectors and (b) with different amplifier gains using all three detectors with different PMT gains ( $0.25$ ,  $0.22$ , and  $0.13 \times 10^6$ ). The coincidence resolving time of 312 ps was obtained with the optimal setup (threshold of 5% of the average 511-keV pulse peak, high voltage of 1100 V, and the amplifier gain of  $\times 20$ ).

are clearly resolved in the flood image, verifying that the detector is suitable for a high-resolution PET scanner. For quantitative evaluation, the peak-to-valley ratio (PVR) and distance-to-width ratio (DWR) were calculated [37], [38]. In general, if the DWR is higher than 1, the detector is said to be able to separate crystals from each other. The average PVR was 10.73 and the DWR was 4.67 for the detector used in Section III-A.

#### C. Light Output and Energy Resolution

With the detector used in Section III-A., relative light outputs were estimated for 225 crystals. The histograms of relative photo-peaks are shown in Fig. 5(b). The figure shows an inhomogeneous photo-peak distribution that is mainly due to variations in the anode gain of a PMT and relatively low light collection efficiency at the edges of the PMT.

Energy resolutions were estimated for 225 crystals and the average energy resolution was calculated as 10.38% at 511-keV as shown in Fig. 5(c). In the central region, energy resolutions

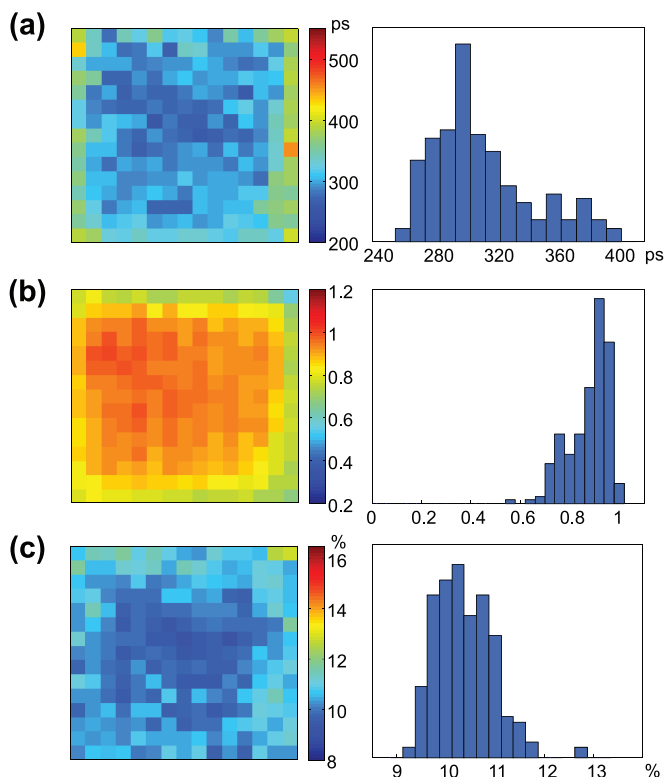


Fig. 5. Two-dimensional and one-dimensional histograms of (a) the coincidence resolving times, (b) the relative photo-peaks, and (c) the energy resolutions for 225 crystals of a sampled detector with the optimal setup.

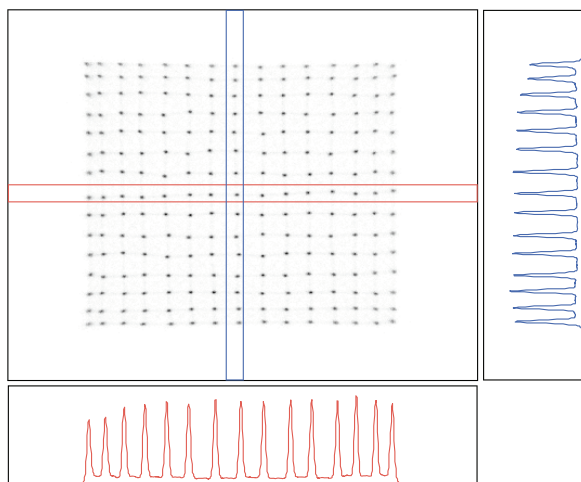


Fig. 6. Flood image and the central vertical and horizontal one-dimensional profiles.

were better than those in the peripheral regions because of the greater number of detected photons.

#### D. Performance of 40 Detectors

The optimal setup acquired from the three randomly selected detectors in Section III-A was applied to all 40 detector modules. The average 511-keV dynode pulse peak voltage of 40 detectors was  $1521 \pm 557$  mV. The flood map quality, energy resolution, and timing resolution of the detectors were estimated employing the reference detector used in Section II-C. The average DWR was  $5.3 \pm 1.0$ . The average timing and energy resolution

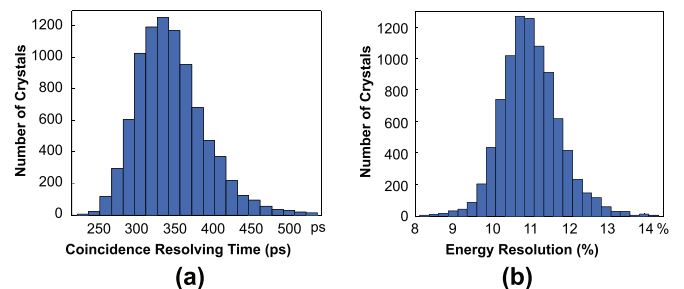


Fig. 7. One-dimensional histogram of (a) the coincidence resolving times and (b) the energy resolutions for 9000 crystals of 40 detectors acquired with the optimal setup.

were 341 ps and 11.04% respectively, and one-dimensional histograms are shown in Fig. 7(a) and 7(b). Their standard deviations were 45 ps and 0.8% respectively.

Our assumption of the same optimal setup for all detectors would contribute to the variations in dynode pulse peak voltage and timing resolution shown in Fig. 7 because some of them may have different optimal setup. However, these variations would be mainly attributed to the variations in PMT properties, such as collection efficiencies, QEs, and gains. It is noted that the product of the gain and collection efficiency ( $G \cdot CE$ ) and QE (or BSI) are the two dominant factors affecting CRT values of TOF PET detectors [39]. Additionally, the inverse proportionality of the relationships between the CRT and  $G \cdot CE$  and between the CRT and BSI has been reported [28], [39], [40]. The optimization of the developed PET detectors can be demonstrated by investigating the relations of CRTs with  $G \cdot CE$ s and BSIs and comparing the relations with the known tendencies reported in the cited references. Fig. 8(a) shows the relationship between CRT and the inverse of the square root of  $G \cdot CE \cdot BSI$ . Each point represents the average result of 225 crystals in each detector. Also, the dependencies of CRTs on each of  $G \cdot CE$  and BSI were examined by selecting only 15 PMTs with similar BSI or  $G \cdot CE$  values respectively. Fig. 8(b) and 8(c) show the relationships between CRT and the inverse of the square root of  $G \cdot CE$  and BSI each. In the figures, proportionality was observed in accordance with previous knowledge, which indicates that the performance of the detector modules was well investigated and a prototype TOF PET system with fine time performance can be realized.

#### IV. DISCUSSION AND CONCLUSION

In this study, we developed PET detector modules designed for a proof-of-concept prototype of a TOF PET scanner based on the advanced multi-anode PMT, H10966A-100, coupled with LGSO scintillation crystals having a smaller cross section ( $3 \text{ mm} \times 3 \text{ mm} \times 20 \text{ mm}$ ) than those used in most current clinical PET scanners. Compact dedicated front-end analog electronics combined with the high packing density and large effective area of the PMT allow a modular detector design such that the scanner will be flexible and extendible with moderate cost. We optimized the parameters (trigger threshold level, high voltage of PMTs, and amplifier gain) to yield the best timing resolution and to facilitate the advantages of excellent time performance of the PMT. The results obtained with the optimal setup derived

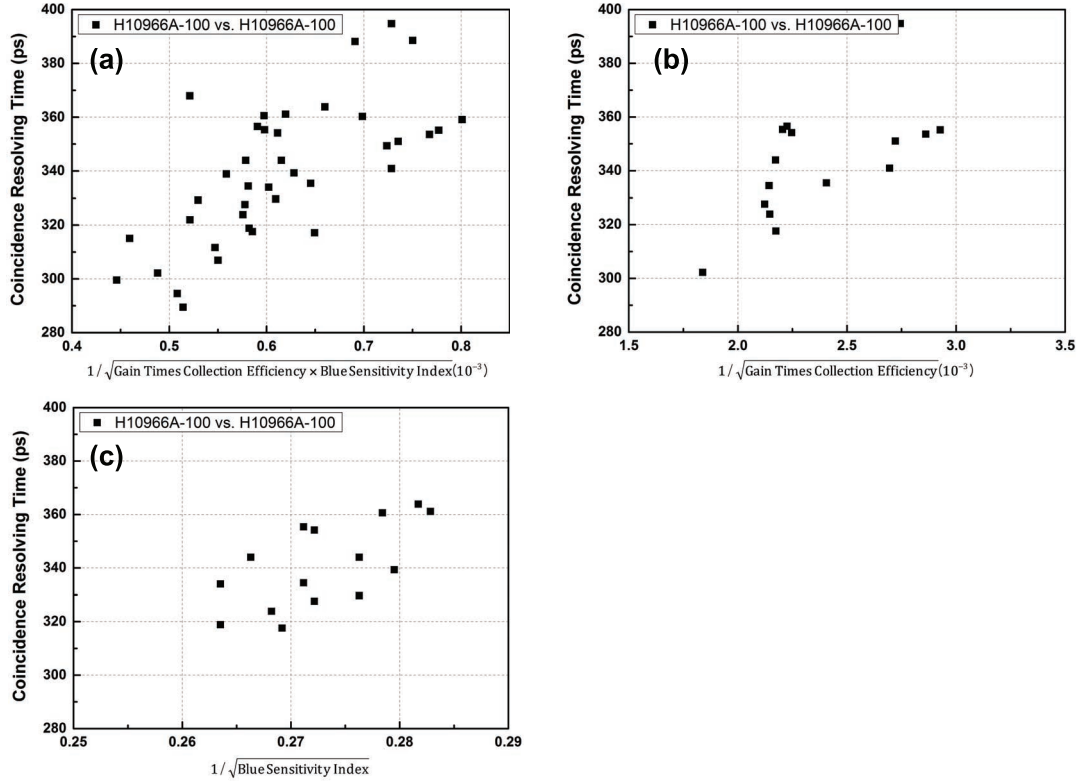


Fig. 8. (a) Coincidence resolving time of 40 detectors (average value of 225 crystals in each detector) according to the inverse of the square root of gain multiplied by collection efficiency and blue sensitivity index of the PMTs. Coincidence resolving time of 15 detectors (b) with similar blue sensitivity indexes according to the inverse of the square root of the  $G \cdot CE$  and (c) with similar  $G \cdot CE$  values according to the inverse of the square root of the blue sensitivity index.

in Section III-A demonstrated that excellent timing resolution, energy resolution, and flood map quality can be achieved with the optimal setup; the average CRTs and energy resolutions for 40 detectors were  $341 \pm 45$  ps and  $11.04 \pm 0.80\%$  respectively, and the average DWR was  $5.3 \pm 1.0$ . In comparison with current clinical whole-body TOF PET/CT scanners based on PMTs (CRTs between 450 ps and 600 ps, energy resolutions between 11.5% and 12.5%, and cross sections of scintillators of  $2.35 \text{ mm} \times 2.35 \text{ mm}$  [19],  $4 \text{ mm} \times 4 \text{ mm}$  [17], [23]–[25] and  $4.2 \text{ mm} \times 6.3 \text{ mm}$  [18]), the developed detectors are expected to yield much better time performance, energy, and spatial resolutions on the system level. A better energy resolution is maintained despite the smaller cross section of scintillators because of the higher number of scintillation photons detected by SBA photocathodes [21], [22]. With good energy resolution, fewer scattered events would be included without the loss of true events by narrowing the energy window, leading to further improved time performance. In comparison with recently developed clinical scanners based on analog or digital SiPMs (CRTs between 325 ps and 400 ps, energy resolutions between 10.5% and 11.1%, and cross sections of scintillators of  $4 \text{ mm} \times 4 \text{ mm}$  [26] and  $3.95 \text{ mm} \times 5.3 \text{ mm}$  [27]), the developed detectors in this study showed comparable timing and energy performance with smaller crystals ( $3 \text{ mm} \times 3 \text{ mm}$ ). In addition, we will be able to use high DWR values (distant and narrow crystal positions) of developed detectors for DOI encoding techniques based on relative offset or light sharing methods [41]–[46] without losing the ability of crystal identification. Accordingly, the developed detector will potentially satisfy

the requirements of a future PET detector with the concurrent measurement of DOI and TOF information.

In general, the PMTs with higher blue sensitivity index and lower transit time jitter yield better time performance of PET detectors based on them [47], [48]. By using H10966A-100, the advanced high-QE multi-anode PMTs with low transit time jitter, we achieved excellent crystal identification, energy, and timing resolutions. Recent studies using normal-QE multi-anode PMTs with clinical-sized Lu-based crystals (cross section between  $2.9 \text{ mm} \times 2.9 \text{ mm}$  and  $3.2 \text{ mm} \times 3.2 \text{ mm}$ ; length between 20 mm and 26 mm) have shown timing resolutions between 380 and 442 ps (442 ps was measured using a large number of detectors [ $n = 48$ ] [49]–[51]). On the contrary, another recent study reported comparable timing resolution (i.e., 348 ps) to the average timing resolution obtained in this study (i.e., 341 ps) using a normal-QE multi-anode PMT and a LYSO array with smaller size ( $1.5 \text{ mm} \times 1.5 \text{ mm} \times 15 \text{ mm}$ ) [52]. A limitation of this study is that we did not directly compare the performances of high- versus normal-QE multi-anode PMT-based PET detectors with same crystal block and readout electronics setup. Therefore, further investigation to clarify the quantitative benefit of better transit time jitter and QE would be necessary.

Recent studies have reported timing resolutions between 200 and 250 ps using single-anode PMTs and fast scintillators [28], [39], [48], [53], [54]. The major reason for the better timing resolution compared with that of the detector developed in this study is the short path length of light transport in the scintillator to the PMT achieved by using short ( $\sim 10 \text{ mm}$ ) scintil-

lators or by coupling the side face rather than the end face of the scintillators. However, for clinical use, such detector configurations are not suitable mainly because of the low sensitivity and wide gap between scintillators. In contrast, the dimensions of the scintillation crystal used in this study were 3 mm × 3 mm × 20 mm, leading to high sensitivity and high spatial resolution, and the detector is thus appropriate for clinical TOF applications. It should be also noted that we measured the performance of detectors almost in system level using FPGA-based TDC and DAQ system that we have developed for TOF PET system implementation.

Our next milestone will be to build a proof-of-concept prototype whole-body PET scanner based on the developed detector modules. In addition, to fully exploit the superb DWR or sparse flood histograms, a DOI encoding capability will be added to the detectors without sacrificing TOF information for the next-generation TOF PET scanner. In this way, it will be possible to further improve the timing and energy resolution from the depth-dependent analysis. Also, baseline and gain corrections of dynode pulses obtained from a waveform digitizer would be another way to improve the results.

#### ACKNOWLEDGMENT

This work was supported by grants from the National Research Foundation of Korea (NRF) funded by the Korean Ministry of Science, ICT and Future Planning (Grant no. NRF-2014M3C7034000), and the Korea Health Technology R&D Project through the Korea Health Industry Development Institute (KHIDI), funded by the Ministry of Health & Welfare, Korea (Grant no. HI14C1135).

#### REFERENCES

- [1] J. S. Karp, S. Surti, M. E. Daube-Witherspoon, and G. Muehlehner, "Benefit of time-of-flight in PET: Experimental and clinical results," *J. Nucl. Med.*, vol. 49, no. 3, pp. 462–470, Mar. 2008.
- [2] D. J. Kadrmans, M. E. Casey, M. Conti, B. W. Jakoby, C. Lois, and D. W. Townsend, "Impact of time-of-flight on PET tumor detection," *J. Nucl. Med.*, vol. 50, no. 8, pp. 1315–1323, Aug. 2009.
- [3] C. Lois *et al.*, "An assessment of the impact of incorporating time-of-flight information into clinical PET/CT imaging," *J. Nucl. Med.*, vol. 51, no. 2, pp. 237–245, Feb. 2010.
- [4] T. Tomitani, "Image reconstruction and noise evaluation in photon time-of-flight assisted positron emission tomography," *IEEE Trans. Nucl. Sci.*, vol. NS-28, no. 6, pp. 4581–4589, Dec. 1981.
- [5] G. El Fakhri, S. Surti, C. M. Trott, J. Scheuermann, and J. S. Karp, "Improvement in lesion detection with whole-body oncologic time-of-flight PET," *J. Nucl. Med.*, vol. 52, no. 3, pp. 347–353, Mar. 2011.
- [6] M. Conti, "Focus on time-of-flight PET: The benefits of improved time resolution," *Eur. J. Nucl. Med. Mol. Imag.*, vol. 38, no. 6, pp. 1147–1157, Jun. 2011.
- [7] S. Surti and J. S. Karp, "Design considerations for a limited angle, dedicated breast, TOF PET scanner," *Phys. Med. Biol.*, vol. 53, no. 11, pp. 2911–2921, Jun. 2008.
- [8] E. Lee, M. E. Werner, J. S. Karp, and S. Surti, "Design optimization of a TOF, breast PET scanner," *IEEE Trans. Nucl. Sci.*, vol. 60, no. 3, pp. 1645–1652, Jun. 2013.
- [9] A. Rezaei *et al.*, "Simultaneous reconstruction of activity and attenuation in time-of-flight PET," *IEEE Trans. Med. Imag.*, vol. 31, no. 12, pp. 2224–2233, Dec. 2012.
- [10] M. Defrise, A. Rezaei, and J. Nuyts, "Time-of-flight PET data determine the attenuation sinogram up to a constant," *Phys. Med. Biol.*, vol. 57, no. 4, pp. 885–899, Feb. 2012.
- [11] T. F. Budinger, "Time-of-flight positron emission tomography status relative to conventional PET," *J. Nucl. Med.*, vol. 24, no. 1, pp. 73–89, Jan. 1983.
- [12] M. Conti, L. Eriksson, and V. Westerwoudt, "Estimating image quality for future generations of TOF PET scanners," *IEEE Trans. Nucl. Sci.*, vol. 60, no. 1, pp. 87–94, Jan. 2013.
- [13] S. Surti and J. S. Karp, "Experimental evaluation of a simple lesion detection task with time-of-flight PET," *Phys. Med. Biol.*, vol. 54, no. 2, pp. 373–84, Jan. 2009.
- [14] B. J. Pichler, H. F. Wehrl, and M. S. Judenhofer, "Latest advances in molecular imaging instrumentation," *J. Nucl. Med.*, vol. 49, no. Suppl. 2, pp. 5S–23S, Jun. 2008.
- [15] M. Conti, "Improving time resolution in time-of-flight PET," *Nucl. Instrum. Methods Phys. Res. A*, vol. 648, no. Suppl. 1, pp. S194–S198, Aug. 2011.
- [16] W. W. Moses, "Recent advances and future advances in time-of-flight PET," *Nucl. Instrum. Methods Phys. Res. A*, vol. 580, no. 2, pp. 919–924, Oct. 2007.
- [17] B. W. Jakoby, Y. Bercier, M. Conti, M. E. Casey, B. Bendriem, and D. W. Townsend, "Physical and clinical performance of the mCT time-of-flight PET/CT scanner," *Phys. Med. Biol.*, vol. 56, no. 8, pp. 2375–2389, Apr. 2011.
- [18] V. Bettinardi, L. Presotto, E. Rapisarda, M. Picchio, L. Gianolli, and M. C. Gilardi, "Physical performance of the new hybrid PETCT Discovery-690," *Med. Phys.*, vol. 38, no. 10, pp. 5394–5411, Oct. 2011.
- [19] W.-H. Wong *et al.*, "A high-resolution time-of-flight clinical PET detection system using the PMT-quadrant-sharing technology," *J. Nucl. Med.*, vol. 55, no. Suppl. 1, p. 657, May 2014.
- [20] G. Adamo *et al.*, "Silicon photomultipliers signal-to-noise ratio in the continuous wave regime," *IEEE J. Sel. Topics Quantum Electron.*, vol. 20, no. 6, pp. 284–290, Aug. 2014.
- [21] Y. Hirano *et al.*, "Performance evaluation of a depth-of-interaction detector by use of position-sensitive PMT with a super-bialkali photocathode," *Radiol. Phys. Technol.*, vol. 7, no. 1, pp. 57–66, Jan. 2014.
- [22] S. Yamamoto, H. Watabe, K. Kato, and J. Hatazawa, "Performance comparison of high quantum efficiency and normal quantum efficiency photomultiplier tubes and position sensitive photomultiplier tubes for high resolution PET and SPECT detectors," *Med. Phys.*, vol. 39, no. 11, pp. 6900–6907, Nov. 2012.
- [23] H. Zaidi *et al.*, "Design and performance evaluation of a whole-body Ingenuity TF PET-MRI system," *Phys. Med. Biol.*, vol. 56, no. 10, pp. 3091–3106, May 2011.
- [24] S. Surti, A. Kuhn, M. E. Werner, A. E. Perkins, J. Kolthammer, and J. S. Karp, "Performance of philips gemini TF PET/CT scanner with special consideration for its time-of-flight imaging capabilities," *J. Nucl. Med.*, vol. 48, no. 3, pp. 471–480, Mar. 2007.
- [25] G.-C. Wang *et al.*, "PET timing performance measurement method using NEMA NEC phantom," in *Proc. IEEE Nucl. Sci. Symp. Med. Imag. Conf.*, Seoul, Korea, 2013, pp. 1–4.
- [26] M. Miller *et al.*, "Characterization of the Vereos digital photon counting PET system," *J. Nucl. Med.*, vol. 56, no. Suppl. 3, p. 434, May 2015.
- [27] C. S. Levin, G. Glover, T. Deller, D. McDaniel, W. Peterson, and S. H. Maramraju, "Prototype time-of-flight PET ring integrated with a 3T MRI system for simultaneous whole-body PET/MR imaging," *J. Nucl. Med.*, vol. 54, no. Suppl. 2, p. 148, May 2013.
- [28] M. Ito, J. P. Lee, and J. S. Lee, "Timing performance study of new fast PMTs with LYSO for time-of-flight PET," *IEEE Trans. Nucl. Sci.*, vol. 60, no. 1, pp. 30–37, Feb. 2013.
- [29] D. V. O'Connor, "Photomultipliers," in *Time-Correlated Single Photon Counting*, 1st Ed. ed. Waltham, MA, USA: Academic, 1984, ch. 4, pp. 103–131.
- [30] C. M. Lee *et al.*, "A novel compensation method for the anode gain non-uniformity of multi-anode photomultiplier tubes," *Phys. Med. Biol.*, vol. 57, no. 1, pp. 191–207, Jan. 2012.
- [31] S. Siegel, R. W. Silverman, S. Yiping, and S. R. Cherry, "Simple charge division readouts for imaging scintillator arrays using a multi-channel PMT," *IEEE Trans. Nucl. Sci.*, vol. 43, no. 3, pp. 1634–1641, Jun. 1996.
- [32] S. I. Kwon *et al.*, "Development of position encoding circuit for a multi-anode position sensitive photomultiplier tube," *Nucl. Med. Mol. Imag.*, vol. 42, no. 6, pp. 469–477, Dec. 2008.
- [33] H. S. Yoon *et al.*, "Initial results of simultaneous PET/MRI experiments with an MRI-compatible silicon photomultiplier PET scanner," *J. Nucl. Med.*, vol. 53, no. 4, pp. 608–14, Apr. 2012.
- [34] G. B. Ko *et al.*, "Development of a front-end analog circuit for multi-channel SiPM readout and performance verification for various PET detector designs," *Nucl. Instrum. Methods Phys. Res. A*, vol. 703, pp. 38–44, Mar. 2013.

- [35] J. Y. Won, S. I. Kwon, H. S. Yoon, G. B. Ko, J.-W. Son, and J. S. Lee, "Dual-phase tapped-delay-line time-to-digital converter with on-the-fly calibration implemented in 40 nm FPGA," *IEEE Trans. Biomed. Circuits Syst.*, Mar. 2015 [Online]. Available: <http://ieeexplore.ieee.org>
- [36] H. S. Yoon, "Network based high performance data acquisition system for PET scanner," Ph.D. dissertation, Dept. Biomed. Sci., Seoul Natl. Univ., Seoul, Korea, 2015.
- [37] F. W. Lau, A. Vandenbroucke, P. D. Reynolds, P. D. Olcott, M. A. Horowitz, and C. S. Levin, "Analog signal multiplexing for PSAPD-based PET detectors: Simulation and experimental validation," *Phys. Med. Biol.*, vol. 55, no. 23, pp. 7149–7174, Dec. 2010.
- [38] J. Du *et al.*, "A simple capacitive charge-division readout for position-sensitive solid-state photomultiplier arrays," *IEEE Trans. Nucl. Sci.*, vol. 60, no. 5, pp. 3188–3197, Oct. 2013.
- [39] Q. Peng, W. S. Choong, and W. W. Moses, "Evaluation of the timing properties of a high quantum efficiency photomultiplier tube," *IEEE Trans. Nucl. Sci.*, vol. 60, no. 5, pp. 3212–3219, Oct. 2013.
- [40] M. Conti, L. Eriksson, H. Rothfuss, and C. L. Melcher, "Comparison of fast scintillators with TOF PET potential," *IEEE Trans. Nucl. Sci.*, vol. 56, no. 3, pp. 926–933, Jun. 2009.
- [41] M. Ito, S. J. Hong, and J. S. Lee, "Positron emission tomography (PET) detectors with depth-of- interaction (DOI) capability," *Biomed. Eng. Lett.*, vol. 1, no. 2, pp. 70–81, Jun. 2011.
- [42] H. Liu, T. Omura, M. Watanabe, and T. Yamashita, "Development of a depth of interaction detector for  $\gamma$ -rays," *Nucl. Instrum. Methods Phys. Res. A*, vol. 459, no. 1–2, pp. 182–190, Feb. 2001.
- [43] N. Zhang, C. J. Thompson, D. Togane, F. Cayouette, and K. Q. Nguyen, "Anode position and last dynode timing circuits for dual-layer BGO scintillator with PS-PMT based modular PET detectors," *IEEE Trans. Nucl. Sci.*, vol. 49, no. 5, pp. 2203–2207, Oct. 2002.
- [44] M. Ito *et al.*, "A four-layer DOI detector with a relative offset for use in an animal PET system," *IEEE Trans. Nucl. Sci.*, vol. 57, no. 3, pp. 976–981, Jun. 2010.
- [45] T. Tsuda *et al.*, "A four-layer depth of interaction detector block for small animal PET," *IEEE Trans. Nucl. Sci.*, vol. 51, no. 5, pp. 2537–2542, Oct. 2004.
- [46] N. Inadama *et al.*, "8-layer DOI encoding of 3-dimensional crystal array," *IEEE Trans. Nucl. Sci.*, vol. 53, no. 5, pp. 2523–2528, Oct. 2006.
- [47] T. Szczesniak, M. Moszynski, L. Swiderski, A. Nassalski, P. Lavoute, and M. Kapusta, "Fast photomultipliers for TOF PET," in *IEEE Nucl. Sci. Symp. Med. Imag. Conf.*, Honolulu, HI, USA, 2007, pp. 2651–2659.
- [48] W. W. Moses *et al.*, "Optimization of a LSO-based detector module for time-of-flight PET," *IEEE Trans. Nucl. Sci.*, vol. 57, no. 3, pp. 1570–1576, Jun. 2010.
- [49] G. B. Ko and J. S. Lee, "Performance characterization of high quantum efficiency metal package photomultiplier tubes for time-of-flight and high-resolution PET applications," *Med. Phys.*, vol. 42, no. 1, pp. 510–520, Jan. 2015.
- [50] M. Nakazawa *et al.*, "Development of a prototype DOI-TOF-PET scanner," in *Proc. IEEE Nucl. Sci. Symp. Med. Imag. Conf.*, Knoxville, TN, USA, 2010, pp. 2077–2080.
- [51] J.-H. Liu *et al.*, "Investigation of the time performance of a LYSO array for TOF-PET," in *arXiv, arXiv:1507.04429*, Jul. 2015, pp. 3–7.
- [52] S. Krishnamoorthy *et al.*, "Design and performance of a high spatial resolution, time-of-flight PET detector," *IEEE Trans. Nucl. Sci.*, vol. 61, no. 3, pp. 1092–1098, Jun. 2014.
- [53] C. L. Kim, G.-C. Wang, and S. Dolinsky, "Multi-pixel photon counters for TOF PET detector and its challenges," *IEEE Trans. Nucl. Sci.*, vol. 56, no. 5, pp. 2580–2585, Oct. 2009.
- [54] M. Moszynski *et al.*, "New prospects for time-of-flight PET with LSO scintillators," *IEEE Trans. Nucl. Sci.*, vol. 53, no. 5, pp. 2484–2488, Oct. 2006.